Experimental study on ice-structure interaction phenomena of vertically sided structures

van den Berg, Marnix; Owen, Cody C.; Hendrikse, Hayo

DOI
10.1016/j.coldregions.2022.103628

Publication date
2022

Document Version
Final published version

Published in
Cold Regions Science and Technology

Cold Regions Science and Technology 201 (2022) 103628

Contents lists available at ScienceDirect

Cold Regions Science and Technology

journal homepage: www.elsevier.com/locate/coldregions

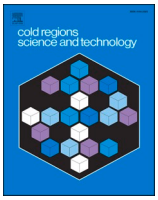

Experimental study on ice-structure interaction phenomena of vertically sided structures

Marnix van den Berg, Cody C. Owen, Hayo Hendrikse *

Delft University of Technology, Faculty of Civil Engineering and Geosciences, Department of Hydraulic Engineering, 2628 CN Delft, the Netherlands

ARTICLE INFO

Keywords:
Continuous brittle crushing
Frequency lock-in
Intermittent crushing
Ice-induced vibrations
Ice basin tests
Real-time hybrid testing

ABSTRACT

This study analyses the results from basin tests with a vertically sided cylindrical pile loaded by ice failing in crushing. Tests were performed with a 'rigid' structure and with structural models representing a series of single-degree-of-freedom (SDOF) oscillators covering a wide range of mass, frequency, and damping values. The structural models were represented by a real-time hybrid test setup, which combined physical and numerical components to measure real ice forces, apply the forces to a numerical structural model, and simulate the dynamics of the tested structural models in real-time. The test results are analysed and simple numerical simulations are performed to assess the relevance of several ice force characteristics observed from the 'rigid' structure tests to the ice-induced vibrations in the SDOF oscillators. The results from the rigid structure tests show that the median ice forcing frequency is linearly related to the ice drift speed. The mean and standard deviation of the ice forces on the rigid structure show a negative force-velocity gradient at low ice drift speeds and indications of a positive force-velocity gradient at higher ice drift speeds. The comparison of experimental results to the simulations of the single-degree-of-freedom oscillator tests shows that the positive force-velocity gradient at higher ice drift speeds allows to best capture the dynamics during continuous brittle crushing as observed in the experiments. Furthermore, the comparison shows that frequency lock-in initiation is primarily driven by the velocity-independent spatial frequency spectrum of the ice force signal. The added damping caused by the positive force-velocity gradient must be considered to capture the frequency lock-in initiation speeds measured in the constant deceleration experiments. The consideration of the negative force-velocity gradient at low relative velocities is not needed to capture these frequency lock-in initiation speeds as observed in the experiments. However, once frequency lock-in is initiated, the negative gradient is needed to correctly capture the dynamics during frequency lock-in. Analysis of the results shows that the peak forces during intermittent crushing at the end of the load build-up phase have a dependence on relative velocity equal to the load dependence on velocity of rigid structures at low speed. This indicates that intermittent crushing is not a purely brittle type of interaction.

1. Introduction

Ice-induced vibrations can be governing for the design of vertically sided structures subjected to ice loads. Structural stresses resulting from ice-induced vibrations can contribute to the fatigue limit state of structures. The potential amplification of ice loads at low ice drift speeds on compliant structures can also be significant for ultimate limit state conditions (ISO, 2019). The mechanisms leading to ice-induced vibrations are not fully understood. Previous studies indicate that the frequency spectrum of time-varying ice loads (e.g., Matlock et al., 1969; Gagnon, 2021; Gagnon, 2012) and the velocity- or rate-dependence of ice strength (e.g., Määttänen, 1978; Kärnä et al., 1999; Yue et al., 2001; Blenkarn, 1970) play a role in the development and severity of ice-induced vibrations. However, there is no agreement on the degree to which both phenomena influence the ice-structure interaction process.

Three types of ice-induced vibrations are distinguished for structures with a single predominant vibration mode excited by the ice: Continuous Brittle Crushing (CBR) at high ice drift speeds, Frequency Lock-in (FLI) at intermediate speeds, and Intermittent Crushing (IC) at low speeds. The ice drift speeds at which the transitions from one mode of interaction to another occur depend on ice and structural properties. Specifically, the mechanisms responsible for the initiation of FLI, an interaction regime characterised by strongly increased structural dynamics, are not well understood. Palmer et al. (2010) suggests that the

* Corresponding author.
E-mail address: h.hendrikse@tudelft.nl (H. Hendrikse).

https://doi.org/10.1016/j.coldregions.2022.103628
Received 24 December 2021; Received in revised form 13 May 2022; Accepted 29 June 2022
Available online 3 July 2022

value of a dimensionless group composed of the ice velocity, ice thickness and the lowest natural frequency of a structure could be predictive for the occurrence of FLI, implying that FLI is a resonance-like phenomenon caused by a failure frequency of the ice, which is linearly related to the ice drift speed and thickness. Ziemer (2021) proposes an analytical condition for FLI initiation based on the force drop at the end of a load build-up phase, suggesting that a dependence of the ice failure forces on the relative velocity is responsible for FLI initiation.

This study aims to clarify the relevance of variance- and frequency-properties and of speed- or rate-dependence of ice forces to dynamic ice structure interaction by analysing ice basin test results and by comparing the test results to numerical simulation results in which the two ice forcing aspects are separated. The specific question of interest is if the characteristics of the ice loads observed on a rigid indenter can be used to explain the ice-induced vibrations of flexible structures.

This study analyses the results of basin tests performed at the Aalto ice basin. The tests were part of a broader test campaign conducted in the summer of 2021. The test campaign was part of the SHIVER project. The data from the test campaign is public, and can be accessed through Hendrikse et al. (2021). This study focusses on the results from tests with a 'rigid' cylinder and tests with a series of single-degree-of-freedom (SDOF) oscillators with a range of mass, stiffness and damping values. The oscillator properties were varied compared to a base case which represents the second global bending mode of an offshore wind turbine on monopile foundation designed for representative Southern Baltic Sea conditions.

The analysed dataset is distinct from other datasets in the ice and structural properties that were tested. The tested natural frequencies of the SDOF oscillators ranged from 0.44 to 6 Hz, with stiffness, mass and damping values each varying with over an order of magnitude. The model ice used in the tests was significantly colder and harder than the model ice that is commonly used in ice basin tests, aiming to replicate the rate dependence of the mean ice load on rigid indenters from ice as observed during the JOIA campaign (Takeuchi et al., 2001). Verification of this approach is treated in (Hendrikse et al., 2022a) which includes a comparison of the rate dependence on the ice load on rigid indenters for traditional and cold model ice, as well as validation tests for existing full-scale structures. The wide range of tested structural properties was enabled by a real-time hybrid test setup (Hammer et al., 2021). This setup combined mechanical and numerical components to simulate the behaviour of a specific test structure in real-time. All SDOF tests described in this study were performed with a constant deceleration, allowing to study regime changes caused by a varying ice drift speed. This test approach resulted in ice-structure interactions in all three interaction regimes (CBR, FLI and IC) for most of the tested combinations of structural properties, leading to a broad and unique dataset.

The experimental design was inspired by experiences from the IVOS test campaign, performed at the Hamburg Ship Model Basin HSVA (Ziemer, 2021). In the IVOS test campaign, tests were performed with higher frequency structures (2.65–7.2 Hz) and 'softer' model ice. Another source of inspiration were the tests by Huang et al. (2007) which are the first tests where the dependence of the interaction on changes in structural properties was systematically tested. Those tests also concerned high natural frequencies (4.29–12.5 Hz) and 'softer' urea ice.

First, we analyse the results from tests with a rigid structure, considering the frequency content, mean and standard deviation of the measured ice forces as a function of ice drift speed. After providing definitions of CBR, FLI and IC as applied in this study, the time-domain results of one of the base case SDOF tests are analysed. Subsequently, a global analysis of all SDOF tests is conducted based on the characteristics of the measured forces and structural dynamics. The analysis focusses mainly on CBR and the mechanisms responsible for FLI initiation. We use simple numerical simulations to test the relevance of several ice forcing characteristics observed in the rigid structure tests to the ice-structure interaction during CBR and the initiation of FLI. Finally, we briefly analyse the interaction in the IC regime, focussing on the observed peak loads.

2. Experimental setup

The experiments were performed at the Aalto ice basin, using a real-time hybrid test setup. The Aalto ice basin is a 40 by 40 m indoor ice basin which can operate with freshwater or ethanol ice. Ethanol ice was used in the tests described in this study. Hendrikse et al. (2022b) gives a detailed description of the experimental design, materials and methods. This section summarizes the most important characteristics of the tests.

The real-time hybrid test setup combined mechanical and numerical components to simulate structural models in real-time. Fig. 1 shows a photo of the setup during testing and gives an overview of the setup components. A cylindrical pile with a diameter of 200 mm penetrated the ice sheet. The pile matched the displacements of the simulated structure at the ice action point. Ice loads were identified from pile strains measured with strain gauges located above the ice action point. The response of the simulated structure to the measured ice loads was numerically simulated on a microcontroller. The calculated structural displacement at the ice action point was applied to the pile by bi-directional linear actuators. The pile displacements were measured by displacement sensors. In the SDOF tests described in this study, only pile displacement in the ice drift direction was modelled.

The real-time hybrid test setup was mounted to a carriage. The carriage was mounted to a bridge spanning the ice tank. Ice drift was simulated by moving the carriage along the bridge with pre-defined speeds. The resulting apparent ice drift (simulated by the moving carriage and the stationary ice sheet) was then opposite to the carriage movement direction. In this article, movement of the carriage is described as ice drift. The real-time hybrid test setup is described as the structure. The measured pile displacements relative to the carriage supporting the real-time hybrid test setup are described as the structural displacements.

During the tests, the global ice forces and structural responses were measured with load cells, strain gauges, accelerometers and displacement sensors. The analyses presented in this study use the unfiltered measured global ice force, and do not convert the measured force to an effective ice pressure or strength. This conversion is avoided to prevent definitional unclarity. Readers interested in (effective) pressure values can convert the presented data based on the diameter of the test pile (200 mm) and the measured ice thickness as available from Hendrikse et al., 2021.

The model ice was created by spraying a fine mist of a water-ethanol mixture on a thin layer of initial ice, according to the following procedure: 1) Lower the tank temperature to -10° C. 2) Remove the ice that has formed on the basin surface. 3) Refreeze the water surface for 20 min, forming a smooth, thin layer of ice. 4) Spray mist at -10 °C for 180 min, forming a layer of sprayed ice of 20 mm. 5) Harden the ice at -11° C for a total of 150 freezing-degree-hours. The spraying water and the water in the ice tank had an ethanol content of 0.3%. The spraying process resulted in a fine grain structure that captured the ethanol in small pockets. The mean ice thickness in which the tests were performed was 30 mm. Where relevant, ice thickness values of specific test runs are mentioned in the data analysis section.

The ice material properties were measured according to the International Towing Tank Conference recommended procedures and guidelines (ITTC, 2014). The flexural (σ_f) and compressive (σ_c) strengths of the ice were measured at the end of each test day. The Young's modulus (E) was only measured on the 17th of June (of the three test days analysed in this study). Table 1 shows the measured material properties. The Young's modulus determination is dependent on the measured ice thickness, causing uncertainty in the measured value. The values between brackets show the Young's modulus variation following from an ice thickness change of ± 5 mm. Please refer to Hendrikse et al. (2022b) for more details on the material property measurements. It is

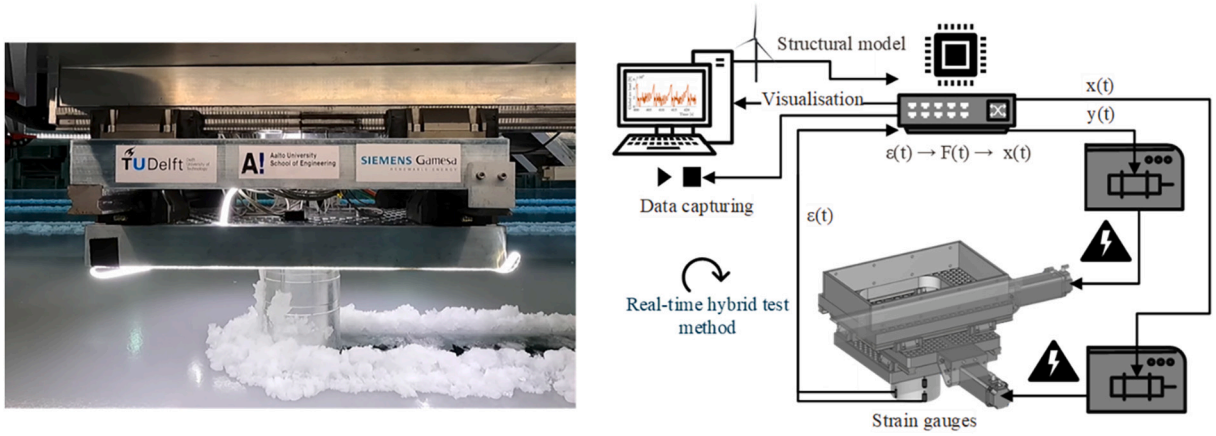

Fig. 1. Left: Photo of the real-time hybrid test setup during testing, showing the cylindrical pile interacting with the ice. Right: Overview of the real-time hybrid test setup (from Hammer et al., 2021).

Table 1
Material properties of the ice on the test days considered in this study. The material properties were measured at the end of the test day.

Ice sheet date	σ_f [kPa]	σ_c [kPa]	E modulus [GPa]
17-6-2021	521	563	13 (7.8–24)
21-6-2021	500	579	–
23-6-2021	444	658	–

noted that the ice material properties are mentioned here only for relative comparison with previous test campaigns, the values may not reflect the properties during actual testing at different moments during the day. Results from the rigid structure tests and results of continuous crushing for the SDOF tests give a good indication of ice strength during testing and, in the view of the authors, provide more relevant information for indentation experiments than the material properties in Table 1.

2.1. Tests with a rigid structure

This study considers 35 tests with a 'rigid' structure, with ice drift speeds ranging from 0.1 to 150 mm s^{-1}. Table 3 (see appendix) gives an overview of the tests with a rigid structure considered in this study. The test IDs represent test identifiers which can be used to obtain the raw test data from the public dataset. The run name contains the test date and the run number. A run is a full passing of the carriage from one side of the basin to the other side. The runs are numbered consecutively starting from 1 on each test day. All tests with a rigid structure performed on the 17th, 21st and 23rd of June are analysed in this study. The test data from rigid tests are used in comparison to the data from the SDOF tests. The SDOF tests were performed in the same ice sheets, or in ice sheets created following the same procedure, as the rigid structure tests. Rigid structure tests from other test days are excluded because the ice conditions were significantly different on those days.

Of course, a perfectly rigid structure cannot be achieved in physical experiments. The term rigid is used to describe tests in which the actuators of the real-time hybrid test setup were in fixed position. Residual flexibility mainly comes from the carriage and bridge to which the setup was mounted and was estimated based on the IC test results to be approximately 0.3 mm kN^{-1}. Analysis of accelerometer data shows that the carriage to which the setup was mounted had a natural frequency between 2.9 and 3.5 Hz.

2.2. SDOF tests

SDOF tests were performed to study the effects of structural properties on the ice-structure interaction processes. The SDOF tests analysed in this study cover a series of mass, frequency and damping ratio variations, taking the second global bending mode of an offshore wind turbine as a base case. The mass, frequency and damping values were varied such that sets of three tests could be constructed in which either the mass, frequency or damping varied, while keeping the other two variables constant, or the mass and frequency varied, while keeping the stiffness and damping ratio constant. Table 2 shows the tested parameter combinations.

Table 4 (see appendix) lists the SDOF tests analysed in this study. The base case (tests 410 and 465) was tested twice. The other tests represent the mass, frequency and damping ratio variations as described above. All SDOF tests considered in this study were performed with a constant-deceleration carriage speed profile. The initial ice drift speeds and test durations are listed in Table 4. During a test, the ice drift speed would go from its initial value to zero in the duration as listed in the table.

3. The influence of ice drift speed on the ice force characteristics on a rigid cylinder

The ice forces on a rigid cylinder for the range of tested ice drift speeds are compared by their frequency content, mean value and standard deviation. A linear drift speed – force frequency relationship, and a frequency dependence on ice thickness, is described by Sodhi and Morris (1986). Sodhi and Morris identify the *characteristic* frequency, which is the peak frequency in the PSD of ice loads, and analyse the dependence between characteristic frequency and ice drift speed. Specific characteristic frequencies were not apparent in the ice load data of our rigid structure tests. Fig. 2 shows the frequency and area-normalized PSDs of rigid structure tests at three different speeds from run 2306_1. The PSDs are filtered for clarity using Barlett's method with five data segments. If a characteristic ice forcing frequency would be present, Fig. 2 would show peak frequencies at the same normalized value.

Instead of using the *characteristic frequency,* the frequency content of the measured ice forces are here compared by their *median frequencies*. The median frequency is defined as the frequency at which half the area of the ice force Power Spectral Density (PSD) is below that frequency:

$$\int_0^{\widetilde{f}} P(f)df = \int_{\widetilde{f}}^{\frac{1}{2}f_s} P(f)df = \frac{1}{2}\int_0^{\infty} P(f)df \tag{1}$$

Where P is the PSD of the mean-normalized ice force signal, $\frac{1}{2}f_s$ is the Nyquist frequency (half the sampling rate f_s, with $f_s = 2000$ Hz) and $\widetilde{f}$ is the median frequency.

Fig. 3 plots the median frequencies of the analysed rigid structure tests against the ice drift speed. The left figure shows the median frequencies of all tests, and the right figure details the results at low ice drift

Table 2
Tested variations of mass, frequency and damping ratio. Mass in 10^3kg, stiffness in kN m^{-1}, frequency in rad s^{-1} and damping as a percentage of critical damping.

	Varying mass			Varying damping	Varying frequency	Varying mass + frequency (const. stiffness)	
Const.	$\omega = 2.76$ $\zeta = 1.3\%$	$\omega = 5.53$ $\zeta = 1.3\%$	$\omega = 12.63$ $\zeta = 1.3\%$	$\omega = 5.53$ $m = 5.02$	$m = 5.02$ $\zeta = 1.3\%$	$\zeta = 1.3\%$ ($k = 156.5$)	$\zeta = 1.3\%$ ($k = 1565$)
varying	$m = 5.02$	$m = 1.25$	$m = 0.99$	$\zeta = 0.17\%$	$\omega = 2.76$	$m = 0.99$ $\omega = 12.63$	$m = 1.10$ $\omega = 37.50$
	$m = 20.06$	$m = 5.02$	$m = 5.02$	$\zeta = 1.3\%$	$\omega = 5.53$	$m = 5.02$ $\omega = 5.53$	$m = 9.9$ $\omega = 12.63$
	$m = 200.6$	$m = 20.06$	$m = 9.9$	$\zeta = 10.6\%$	$\omega = 12.63$ $\omega = 37.50$	$m = 20.06$ $\omega = 2.76$	$m = 200.6$ $\omega = 2.76$

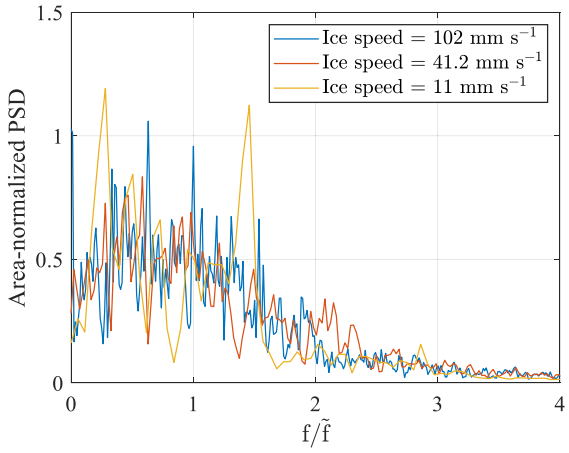

Fig. 2. Frequency and area normalized PSDs at three different ice speeds, from the same test run. The frequencies are normalized using the median frequencies $\tilde{f}$, which are different for each speed.

speeds. A distinction is made between tests from different test runs. Tests from a single run are all performed within a short time interval and the ice conditions are assumed to be constant for these tests. There is a clear relationship between the drift speed and the median force frequency. In the speed range analysed in this study, the relationship appears to be linear. A linear relationship between the temporal forcing frequency and drift speed indicates that the spatial frequency of the ice force (i.e., the ice force variation per unit of crushed length) is speed independent.

Figs. 4 and 5 show the mean ice force and the force standard deviation as a function of ice drift speed, respectively. The mean force and force standard deviation are influenced by the ice drift speed. At low ice drift speeds, both the mean force and the force standard deviation decrease with an increasing drift speed. The force-velocity gradient is steepest at speeds close to zero, between 0.1 and ~ 3 mm s^{-1}. Note that the mean and standard deviation of the test with a speed of 0.1 mm s^{-1} lay outside the axis limits. At high ice drift speeds, the mean and standard deviation seem to have a weak positive correlation with drift speed, though further testing at higher speeds is necessary to confirm this. The transition from a decreasing mean ice load with increasing drift speed to an increasing mean ice load occurs at a drift speed of approximately 20 mm s^{-1} when looking at the data in Fig. 4. This is not a fixed value and expected to be strongly dependent on the temperature of the ice, among other properties. The mean force and force standard deviation appear to be related to the ice thickness (h) and the time-of-day at which the tests were conducted, which could indicate strength or temperature dependencies. Tests performed at the end of a test day (with a higher run number), and with the highest ice thickness, show the highest mean ice force and force standard deviation.

The increase of mean ice force for lower ice drift speeds is in accordance with previous observations (e.g., Hendrikse et al., 2018; Sodhi et al., 1998), and is often linked to more ductile behaviour at low loading rates. The increase in forces at high drift speeds has also been observed earlier (e.g., Blenkarn (1970) and Kärnä et al. (1993)), though at higher speeds than tested here. Hendrikse et al. (2018) also observed a positive mean force-drift speed gradient at higher ice drift speeds in an experimental setup that was similar to the setup used in the tests analysed in this study. They analysed local ice pressure data from tactile sensors and showed that the positive gradient disappears when removing the force contributions from pressure cells with a low pressure. It was hypothesized that the force contribution from cells with a low local pressure is related to clearing of crushed ice.

4. Definitions of CBR, FLI and IC adopted in this study

For the intercomparison and classification of the measured data from the SDOF oscillator tests, we adopt definitions of CBR, FLI and IC that are generally aligned with the definitions used in the ISO standard (ISO,

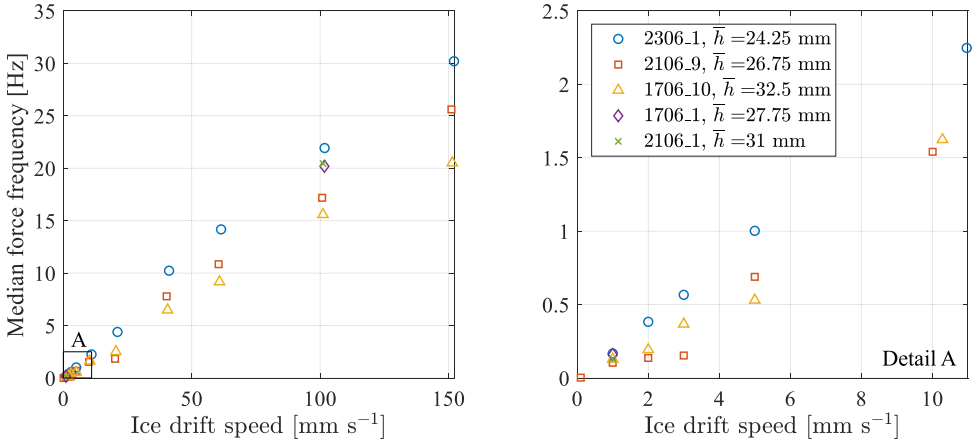

Fig. 3. Median ice force frequency as a function of drift speed.

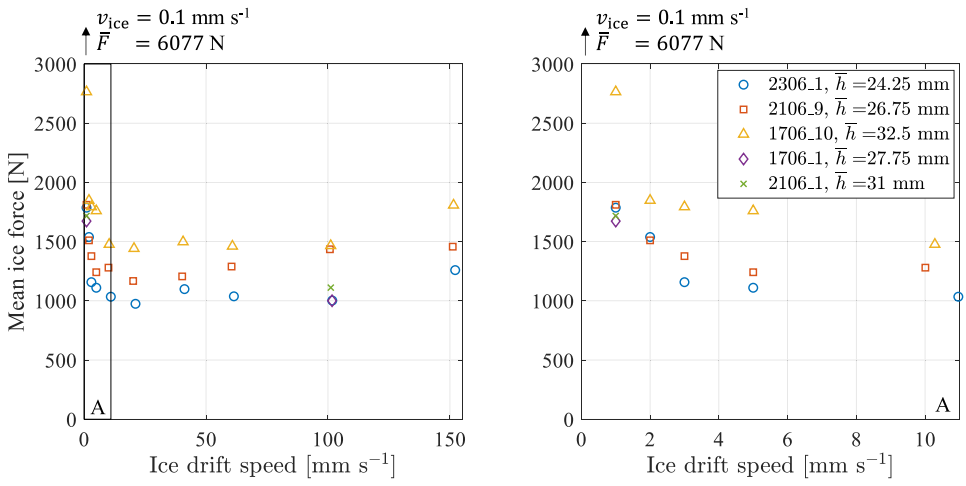

Fig. 4. Mean ice force as a function of ice drift speed.

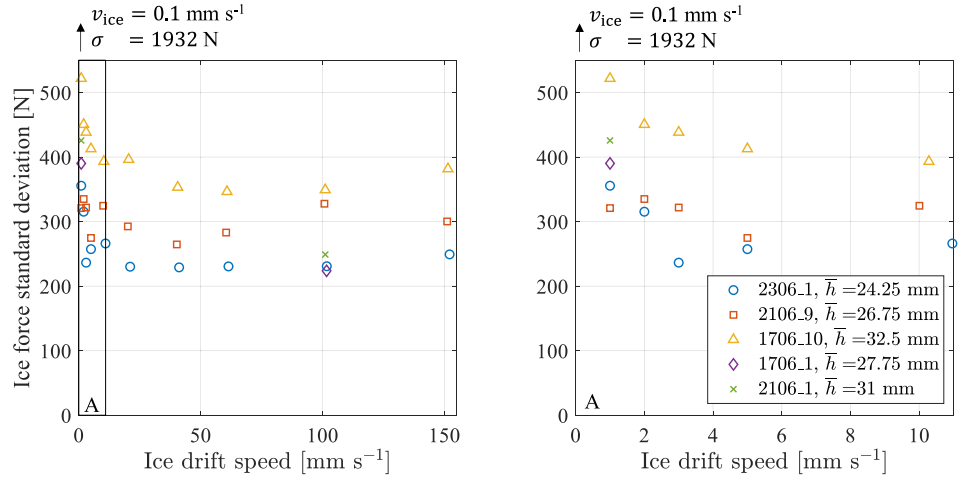

Fig. 5. Ice force standard deviation as a function of ice drift speed.

2019) and in scientific literature. The dataset analysed in this study shows that there is often an intermediate time interval when transitioning from one interaction regime to another, in which the ice-structure interaction process shows attributes of multiple interaction regimes. This makes the formulation of specific strict definitions somewhat arbitrary. Nevertheless, such definitions are adopted here to enable an unbiased automated comparison and classification of the test data. The definitions adopted in this study are applicable to SDOF oscillators or structures with a single dominant vibration mode.

Interaction at ice drift speeds higher than the speed at which FLI first occurs, with FLI as defined below, are classified as CBR. All SDOF tests analysed in this study were performed with a constant deceleration ice drift speed profile. To avoid considering interaction behaviour that occurs in the transition to FLI, we selected test intervals with speeds significantly above the FLI initiation ice drift speed when assessing interaction during CBR. Typically, a time interval between 20 and 40 s after the start of the test is selected for analysis of CBR interaction. The first 20 s are excluded to reduce the possible influence of initial conditions on the results. At 40 s, the ice drift speed is on average 37 mm s^{-1} above the FLI initiation speed and at a minimum 12 mm s^{-1} above the FLI initiation speed.

The two most common definitions of FLI are based on the failure frequency of the ice and the relative velocity between ice and structure. The ISO standard (ISO, 2019) adopts a failure-frequency based definition, stating that in FLI, 'the ice failure frequency in crushing adapts to one of the lowest natural frequencies of the structure.' A relative-velocity based definition was first proposed by Toyama et al. (1983) in the form of the frequency lock-in relation. The frequency lock-in relation states that during FLI, the structural velocity at the location of ice action in each vibration cycle $\dot{u}_{max}$, and the ice drift speed v_{ice} conform to the following relationship:

$$\dot{u}_{max} = \beta v_{ice} \tag{2}$$

Where FLI is commonly defined by a range of β. For instance, Ziemer (2021) considers interaction as FLI for $0.9 < \beta < 1.5$ (among other criteria).

In this study, we use a relative velocity-based definition of FLI and add a consistency and periodicity requirement. Interaction is defined as FLI if:

Five vibration cycles reach a zero or negative relative velocity (i.e., $\beta > 1$) *between ice and structure at the waterline in the ice drift direction, within a period of six times the structural vibration period in free vibration.*

The consistency requirement is added because the experimental results show several occasions where $\beta > 1$ for only one or two cycles, after which the relative velocity would be well above zero for several cycles. According to the definition adopted in this study, these isolated zero-crossings of relative velocity are not considered as FLI. For the tests analysed in this study, a relative-velocity based definition of FLI matches with an ice forcing frequency-based definition. The forcing frequency is influenced by the relative velocity, thus once the relative velocity

between ice and structure starts to reach zero, the forcing frequency starts to synchronize with the vibration frequency of the structure. This is shown in Section 7.2.

In the time between FLI initiation and the end of the test (when reaching an ice drift speed of zero), the interaction transitions from FLI to IC, showing the typical saw-tooth displacement and ice force profiles at low ice drift speeds. In this study, we consider the interaction as IC when the following condition is met:

The duration of structural displacement in the direction of ice drift must be larger than the vibration period of the structure in free vibration.

The analysis shows that this criterion ensures that the loading condition at the peak of a saw-tooth is close to quasi-static.

5. Time domain analysis of SDOF test results

The 14 SDOF oscillators that were tested cover a wide range of structural properties, leading to a diverse set of test results. In most tests, the transitions from CBR to FLI and IC can be distinguished as the ice drift speed decreases. This section discusses the time-domain results of one of the base-case tests as an example. The time-domain results are discussed to aid with the interpretation of the comparisons based on signal characteristics presented in the following sections. Time domain plots for all tests are not included, but can be created from the public dataset.

Fig. 6 shows the time domain result of one of the base-case tests (ID 465). The upper figure shows the structural displacement from its equilibrium position, and the middle figure shows the ice force on the structure. Both force and displacement are unfiltered signals sampled at 2000 Hz. The lower figure shows the relative velocity between ice and structure in the ice drift direction. The relative velocity is computed by subtracting the structural velocity from the ice drift speed. The structural velocity is derived from the structural displacement by taking the time derivative. The resulting pile velocity and the measured carriage speed (i.e., ice drift speed) are filtered with a 5th order Butterworth filter in both directions with a lowpass frequency of 25 Hz. Filtering both in forward and reverse direction prevents the phase shift that would result from filtering in a single direction. The ice drift direction is defined as the positive direction for displacement, force and velocity. In this test, the ice drift speed reduced linearly from a maximum of 70 mm s^{-1} to zero over a duration of 402 s.

The structural dynamics and ice load characteristics clearly change as the ice drift speed reduces. At a high ice drift speed (see also detail A, Fig. 7), the structure vibrates at its natural frequency. The vibration amplitudes are smaller than the vibration amplitudes at lower drift speeds, and the relative velocity between ice and structure is always above zero. The interaction can be described as CBR. At an ice drift speed of ~33 mm s^{-1} the interaction is in the FLI regime. The vibration amplitudes of the structure start to increase significantly (see also detail B, Fig. 8) and the relative velocity between ice and structure drops to or below zero in each vibration cycle. It can be seen that as the ice drift speed reduces the amplitude of oscillation reduces linearly as well (Fig. 6, between 225 and 275 s, approximately), consistent with the lock-in relation in Eq. 2. As the ice drift speed decreases further, the amplitudes of structural motion and ice force start to increase. The force and displacement follow a saw-tooth pattern typical of IC interaction (see also detail C, Fig. 9).

Fig. 7 shows the interaction at an ice drift speed of ~57 mm s^{-1}. There is no apparent influence of the structural vibration on the ice force visible in the time-domain plots. However, further analysis indicates that the ice force is also influenced by the structural dynamics in the CBR regime. This is analysed in Section 7.

Fig. 8 shows the interaction at an ice drift speed of ~33 mm s^{-1}. The influence of the structural vibration is visible in the force signal. In the phase where the structure moves with the ice (a), the ice force signal fluctuates less per unit time than in the periods where the structure moves against the ice drift direction (c). In the phase where the relative velocity is low, a 'bump' can be observed in the relative velocity signal (a). This bump is caused by the ice force peak, which pushes the structure from its free vibration path. When the ice force drops after failure, the structure starts moving against the ice drift direction, causing a higher relative velocity (c). When the structure moves with the ice, the relative velocity often drops below zero, causing a trough in the

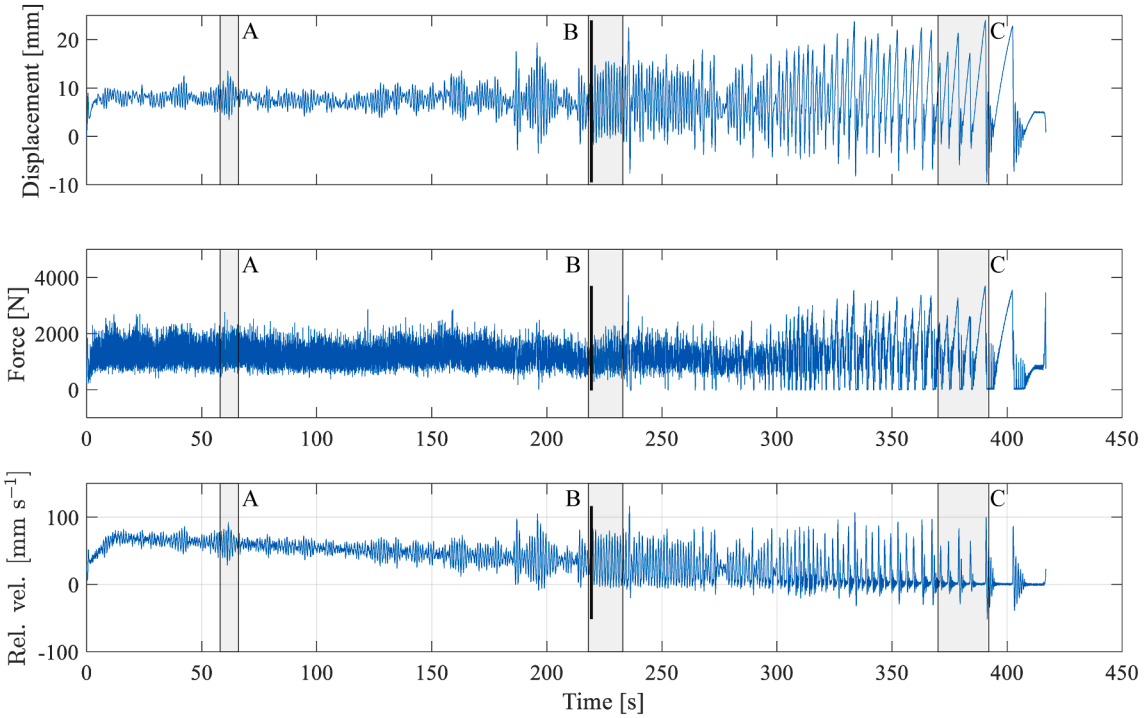

Fig. 6. Time-domain result of test ID 465. Details indicated in grey are plotted in Figs. 7, 8 and 9. The black line indicates a transition to FLI according to the transition definition provided in Section 4.

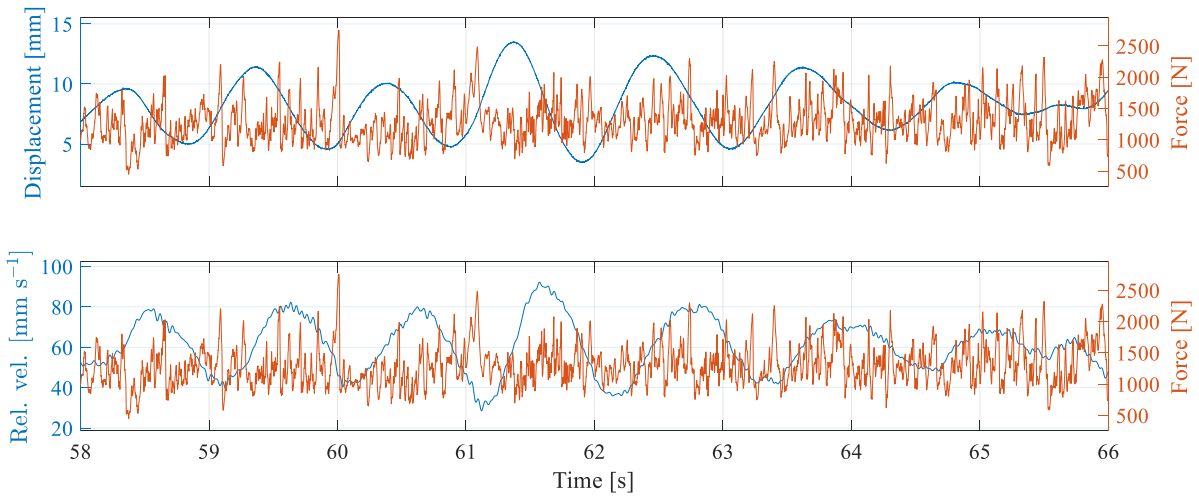

Fig. 7. Detail A: Structural displacement, ice force and relative velocity at an ice drift speed of ~57 mm s^{-1}.

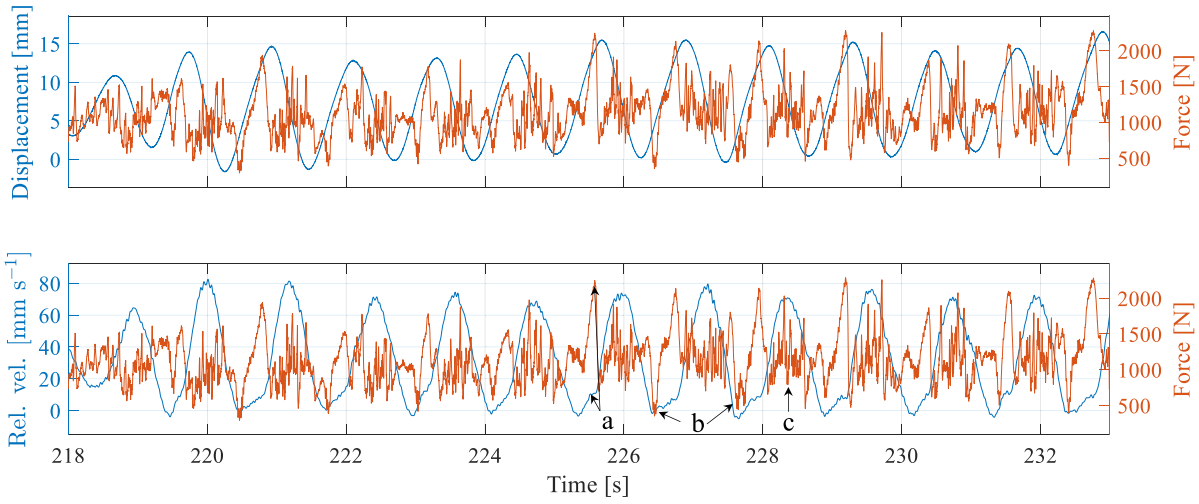

Fig. 8. Structural displacement, ice force and relative velocity at an ice drift speed of ~33 mm s^{-1}.

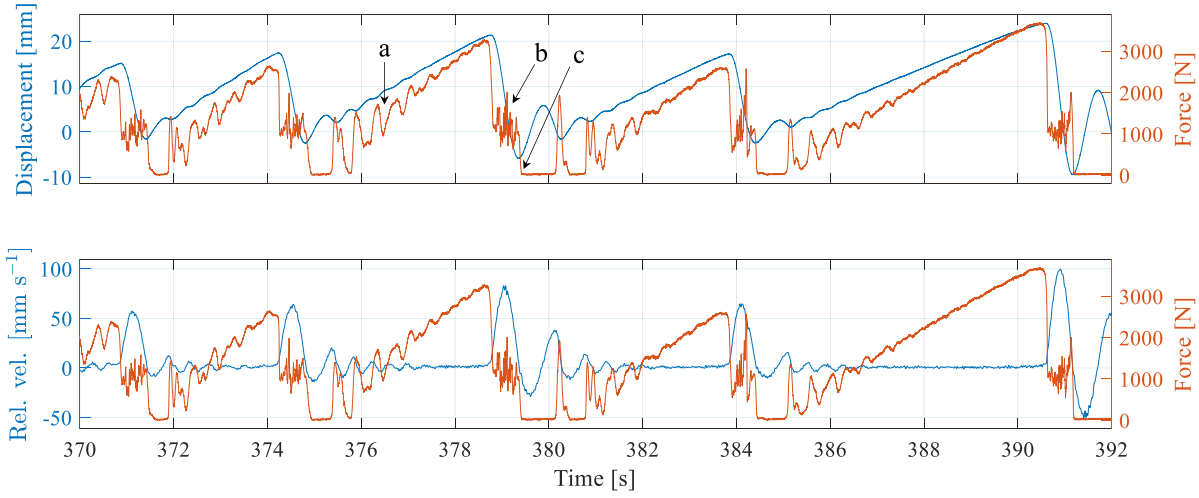

Fig. 9. Structural displacement, ice force and relative velocity at an ice drift speed of ~8–2 mm s^{-1}.

measured ice forces (b). However, the ice force does not drop to zero immediately, indicating that there is elastic unloading of the ice or the residual compliance in the carriage.

Fig. 9 shows the interaction at an ice drift speed between 8 and 2 mm s^{-1}. The ice force and structural displacement follow a saw-tooth pattern. In the load build-up phase (a), the relative velocity between ice and structure is very low. During load build-up, oscillations occur in the force, displacement, and relative velocity signals. These oscillations are the result of the transient response of the SDOF structure from the previous load drop. These oscillations are also observed in full-scale data (e.g., Gagnon, 2021). Gagnon (2021) associates the frequency of these oscillations to an effective mass and spring constant of the ice sheet. The experimental data analysed in this study shows that the oscillation frequency during the IC load build-up phase is above the structure's natural frequency for all tests, supporting a hypothesis of ice sheet effective stiffness contributing to the oscillation frequency.

At the end of the load build-up phase, the vibrations have mostly dissipated, and the loading condition is close to a quasi-static condition. The highest force peaks occur at the end of the load build-up phase. When the force drops, the structure moves against the ice drift direction and the structure crushes through the ice with a higher relative velocity (b). The ice forces in this period are lower than the peak force reached at the end of the load build-up phase. When the relative velocity drops below zero (c), contact loss occurs, which leads to a drop to zero in the measured ice force. Sodhi (1991) obtained similar test results in model-scale SDOF tests in freshwater ice. He also observed the force drops to zero as caused by loss of contact between ice and structure. In the dataset analysed in this study, the contact loss and force drop to zero was only observed for the more compliant structures and did not occur in all tests.

Phase (b), directly after the force drop, in which the ice and structure interact with a high relative velocity, is described by Sodhi (1991) as extrusion of crushed ice. However, in the current test results, this phase is better described as ice crushing (and extrusion) at high relative velocity. The load level in phase (b) is similar to the load levels measured at the higher ice drift speeds. If only extrusion of crushed ice would occur, and not the crushing process itself, one would expect significantly lower loads in this phase. Kärnä et al. (1993) observed that during the spring-back phase, the force drops to a low level immediately after failure (i.e., the force drop at the end of the loading phase), and then starts to increase during the spring-back phase. This behaviour is not consistently observed in the tests analysed in this study.

After having discussed the time-domain results typical for most of the SDOF tests analysed in this study, we now compare the results of all SDOF tests based on the characteristics of the measured forces and the structural dynamics. We start by comparing the results in CBR, after which the analysis focusses on FLI initiation and the interaction characteristics during IC.

6. CBR forces on the SDOF structures in comparison to the forces on the rigid structures

The ice forces measured on the rigid structures are compared against the ice forces on the SDOF structures during CBR. For each SDOF test, the ice forces in the time interval from 20 to 40 s after the start of the test are analysed. The first 20 s of the tests are not considered to eliminate the possible influence of initial conditions. Fig. 10 shows the median frequency, mean and standard deviation of the measured ice forces on the SDOF structures in comparison to the values measured on the rigid structure. The frequency content, mean ice force and force standard deviation on the SDOF structures during CBR are similar to the force properties measured on the rigid structure, indicating that for these force characteristics there is minimal influence of structural motion on the ice forces during CBR.

As mentioned in Section 3, the linear dependence of ice force frequency content on ice drift speed is consistent with a velocity-independent spatial frequency spectrum of the ice force. On the other hand, the results also show that the mean and standard deviation are dependent on the ice drift speed, showing that the interaction velocity does influence these properties.

7. Influence of ice forcing characteristics on the measured structural dynamics in the CBR and FLI regimes

The importance of the spatial frequency and the velocity-dependent properties of the ice forces to the ice-structure interaction during CBR, FLI and the transition from CBR to FLI is tested by performing simple numerical simulations for the set of SDOF oscillators used in the ice basin tests. The purpose of the numerical simulations in this section is not to introduce a novel ice-structure interaction model, but only to test the relevance of the mechanisms commonly considered in literature to the initiation of FLI. With this purpose in mind, the model is kept as simple as possible.

In the simulations, the measured force-displacement signal from one of the rigid structure tests is applied to the SDOF oscillators. The measured force signals are scaled such that the standard deviation matches the standard deviation of the force in CBR of the SDOF test being simulated. First, the signal is applied while not considering any force-velocity dependence (Fig. 10). Then, the signal is applied while considering a positive gradient of the mean ice force with drift speed. Finally, both a positive and the negative ice force gradients with drift speed are considered. The simulations are described by the following

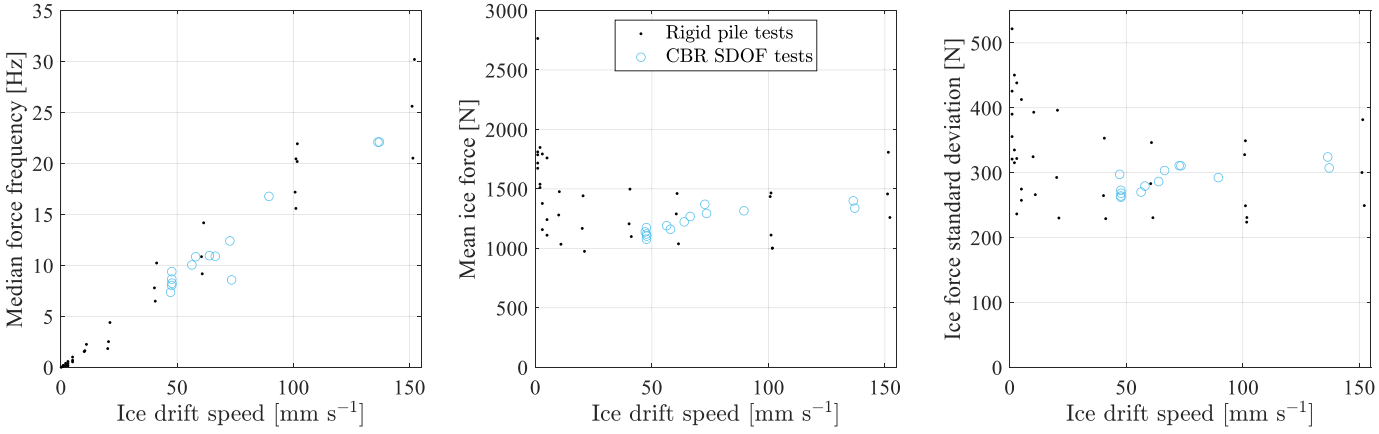

Fig. 10. Comparison of frequency content, mean and standard deviation of ice forces measured on SDOF oscillators during CBR with the loads measured on a rigid structure.

equation:

$$\ddot{w} + 2\zeta\omega_n\dot{w} + \omega_n^2 w = \frac{F(d_{\mathrm{rel}})\alpha(v_{\mathrm{rel}})}{m} \tag{3}$$

in which w is the pile waterline displacement in the ice drift direction and the overdots denote derivatives with respect to time, m, ζ and ω_n are the mass, damping ratio and natural frequency of the tested SDOF oscillators, and $F(d_{\mathrm{rel}})$ is a force-displacement signal obtained from a rigid structure test. The ice displacement during the rigid structure test is estimated as the product of the test duration and the ice drift speed (the ice drift speed was constant during the rigid structure tests). The ice displacement and ice drift speed during the simulated SDOF tests is determined from the linearly varying speed profile as follows:

$$\begin{aligned} v_{\mathrm{ice}} &= v_{\mathrm{init}} + \dot{v}_{\mathrm{ice}}\, t \\ d_{\mathrm{ice}} &= \frac{1}{2}\dot{v}_{\mathrm{ice}}\, t^2 + v_{\mathrm{init}} t \\ \dot{v}_{\mathrm{ice}} &= \frac{v_{\mathrm{init}}}{D} \end{aligned} \tag{4}$$

in which v_{init} is the initial ice drift speed and D is the test duration, as listed in Table 4. The relative displacement and velocity between the ice and structure are then:

$$d_{\mathrm{rel}} = d_{\mathrm{ice}} - w,\ v_{\mathrm{rel}} = v_{\mathrm{ice}} - \dot{w} \tag{5}$$

Furthermore, the ice force F is subject to the following constraints:

$$F \le \frac{v_{ice} - \dot{w}}{dt} m + c\dot{w} + kw \Big|_{\dot{w} \le v_{ice}} \tag{6}$$

$$F = 0|_{\dot{w} > v_{ice}} \tag{7}$$

Eq. [6] states that the ice force F is limited by the force needed to reach a zero relative velocity between ice and structure. Eq. [7] states that the ice force is zero if the structure moves away from the ice. Constraints [6, 7] imply there is no elasticity in the ice, which deviates from the experimental observations as shown in Fig. 8.

The scaling factor α is determined as follows:

$$\alpha(v_{\mathrm{rel}}) = \begin{cases} a_1 v_{\mathrm{rel}} + b_1|_{v_{\mathrm{rel}}<0.02} \\ a_2 v_{\mathrm{rel}} + b_2|_{v_{\mathrm{rel}}>0.02} \end{cases} \tag{8}$$

The parameters a_1, b_1, a_2 and b_2 are varied to test the effect of velocity-dependent ice forces on the ice-structure interaction process. First, $a_1 = a_2 = 0$ and $b_1 = b_2 = 1$, yielding velocity-independent ice forces. Then, a positive mean force-velocity gradient is applied, yielding $a_2 = 1.798$ and $b_2 = 0.964$ (and $a_1 = 0$, $b_2 = 1$). The positive force-velocity gradient is derived by performing a linear least-squares fit to the force-velocity trends observed in the rigid structure tests. Finally, the negative force-velocity gradient at low velocities is linearly approximated by $a_1 = -15$ and $b_1 = 1.3$ (and $a_2 = 1.798$ and $b_2 = 0.964$), yielding a factor 1.3 force increase at zero relative velocity compared to the force at a relative velocity of 20 mm s^{-1}. The simple assumptions applied in these numerical tests assume that the effect of relative velocity on force is instantaneous and not persistent (i.e., the loading history does not affect the ice strength).

To account for the effects of randomness in the force-displacement signals measured on the rigid structures, the simulations are performed with force-displacement signals from three different rigid structure tests with IDs 420, 466 and 472.

The simulation results are compared to the experimental data based on the structural vibration amplitudes in the CBR ice drift speed range, the ice drift speed at which FLI is initiated (according to the definition provided in Section 4), and the vibration amplitudes during FLI. Figs. 11 and Fig. 14 show the simulation results in comparison to the experimental data for the base-case SDOF test ID 465, when applying the force-displacement signal from rigid structure test ID 472.

7.1. The CBR regime

Fig. 11 shows interaction at an ice drift speed of ~65 mm s^{-1}. Although the ice force signals are visually similar, the structure clearly oscillates more strongly in the simulated interactions. The structural oscillations are strongest in the simulation where no force gradient with velocity is considered. This result is in accordance with our expectation,

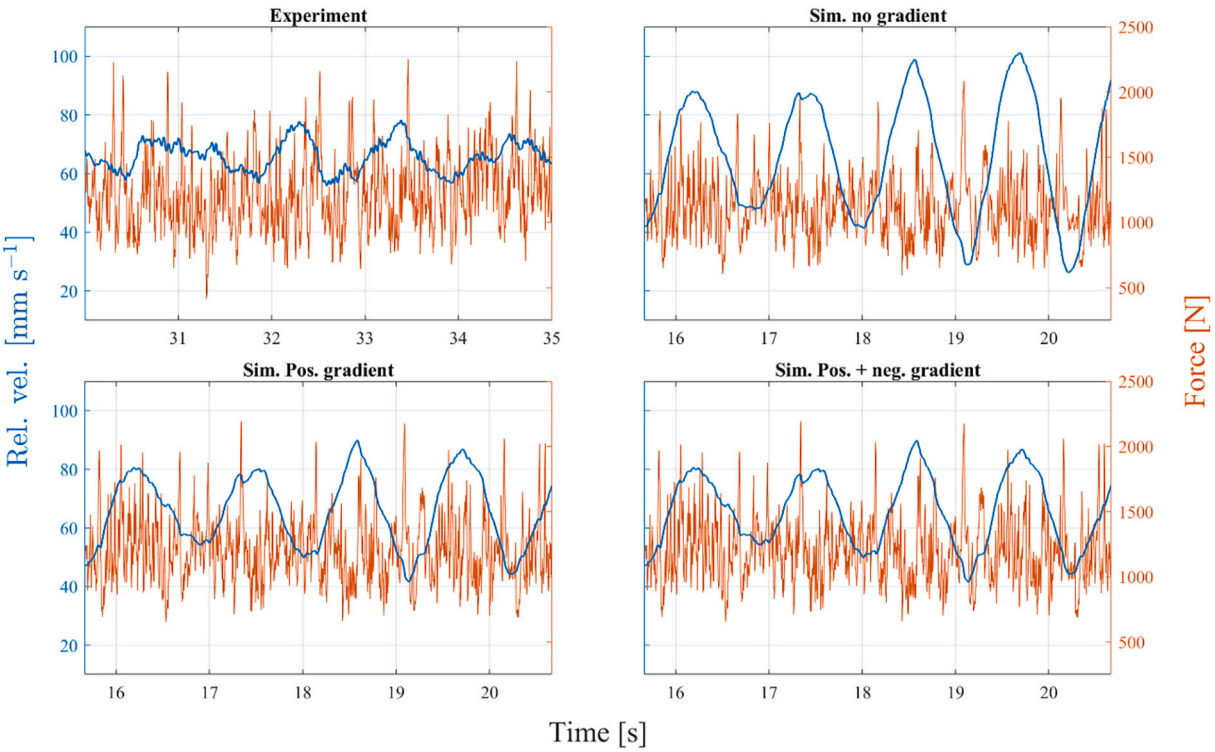

Fig. 11. Time-domain comparison of experimental and simulation results at the same ice drift speed of ~65 mm s^{-1}.

as the positive force-velocity gradient at higher velocities results in added damping. This added damping could originate from, for example, rubble, extrusion of ice or hydrodynamic effects, which are all contained in the global load measurement on the pile. Also, the positive gradient needs further experimental confirmation as discussed before. The negative damping that might result from the negative force-velocity gradient at low velocities does not influence the interaction, as the relative velocity range where this effect is simulated to occur is not reached. The validity and relevance of the simulated ice loading mechanisms are further assessed by comparing the parameterized properties of the time-domain results for all SDOF oscillators.

Fig. 12 shows the mean amplitudes of structural displacement in the period between 20 and 40 s of the experiment and the simulations. The figure shows the experimental results, sorted from low to high, against the simulated results for the three different assumptions on force-velocity dependence. The bars extend from the lowest simulated value to the highest simulated value for the three rigid structure force-displacement signals used. The primary observation from Fig. 12 is that the simulations with no force gradient significantly overestimate the structural oscillations in the CBR regime for several of the tested structural property combinations. The force-velocity gradient effect is especially strong for the structures with low mass and/or stiffness. This can be attributed to the specification of structural damping as a fraction of critical damping. The structures with low mass and stiffness generally have a lower damping value expressed in units of force per velocity, increasing the relative contribution of the effective damping caused by the positive force-velocity gradient. The simulations with a positive, or positive and negative, force-velocity gradient result in displacement amplitudes in the same range as the amplitudes observed in the experiments. Even though the force-displacement signals applied in the numerical simulations have similar means, standard deviations and median frequencies (at the same relative velocity), the amplitudes of structural displacement are still influenced significantly by the specific random variations of the three signals used in the simulations. For most tests, the inclusion of the negative force-velocity gradient does not affect the simulation results at high ice drift speeds, as the relative velocity range at which the negative gradient starts to play a role is often not reached.

The reduction in oscillation amplitudes resulting from the effective damping caused by the positive force-velocity gradient was already discussed by Blenkarn (1970). However, this effect is missing in several numerical models of ice-structure interaction (e.g., Hendrikse and Nord, 2019; Gagnon, 2021). The experimental and numerical data presented in this study indicate that the effective damping resulting from the positive force-velocity gradient may have to be considered in ice-structure interaction models, provided it can be confirmed with dedicated experiments.

The influence of structural oscillations on the measured ice forces in the CBR regime can also be observed in the frequency domain. To demonstrate the influence of structural vibration on the ice load signal, the PSDs of the ice forces in the time interval from 20 to 40 s of experiments and simulations are normalized by the undamped natural frequency of the structure (f_{struc}), are area-normalized, and summed for all the structures. Fig. 13 shows the combined PSD plots of the measured ice forces (left), the simulated ice forces with no force-velocity gradient (middle) and with only a positive force-velocity gradient (right). The measured ice forces show a clear trough at the natural frequency of the structure ($f/f_{struc} = 1$). In the simulation results with no force gradient, this trough is not observed. In the simulation results with a positive force-velocity gradient, a local minimum also occurs at the structure natural frequencies, although the dip is less pronounced than in the PSD of measured forces. The mechanism behind this dip in the frequency content of measured forces at the natural frequency of the structure is currently not understood, but in any case, shows that the force characteristics from rigid structures cannot be directly applied to simulate the dynamics of flexible structures. The validity of the spectral approach currently suggested in ISO19906 can be questioned based on these results.

7.2. The FLI regime

Fig. 14 shows the experimental and simulation results for the first ~6 cycles after initiation of FLI, as defined in Section 4. The ice drift speed at which FLI is initiated is different for all cases, and is further assessed in Fig. 15. The change in ice force frequency content with relative velocity is visible in the experimental results (as discussed in Section 4) and in the simulation results. In the time-domain example shown in Fig. 14, the force signal of the simulation with a positive force-velocity gradient seems to match particularly poorly with the measured force signal. This obervation should be considered an outlier, and does not extend to the positive force gradient simulations in general, as the correct predictions of the FLI initiation speeds from this model type in Fig. 15 indicate.

Fig. 15 shows the ice drift speeds at which FLI is initiated. In the simulations with no force-velocity gradient, FLI is initiated at higher ice drift speeds than the FLI initiation drift speeds observed in the experiments. Simulations with a positive or with a positive and negative force gradient result in FLI initiation speeds closer to the results of the experiments. For tests with a low FLI initiation speed, the simulations with no gradient and with only a positive gradient predict the FLI initiation speed even better than the simulations with a positive and negative force gradient.

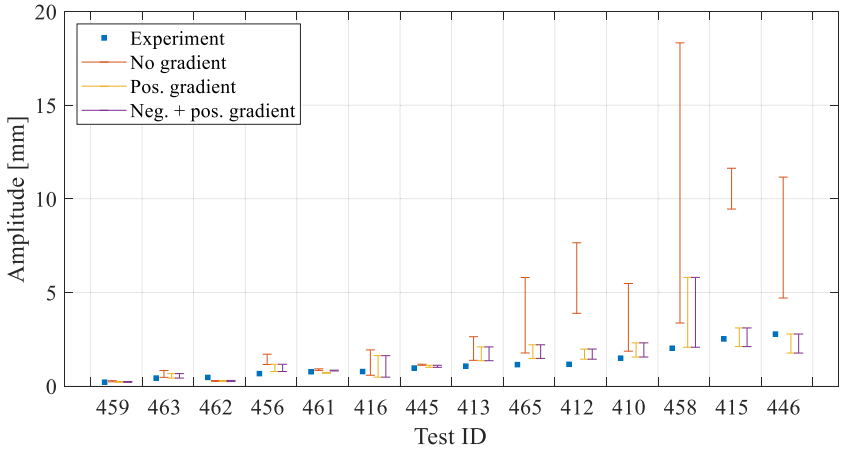

Fig. 12. Mean structural displacement amplitudes during CBR. Comparison of experiments (blue) and simulations. (For interpretation of the references to colour in this figure legend, the reader is referred to the web version of this article.)

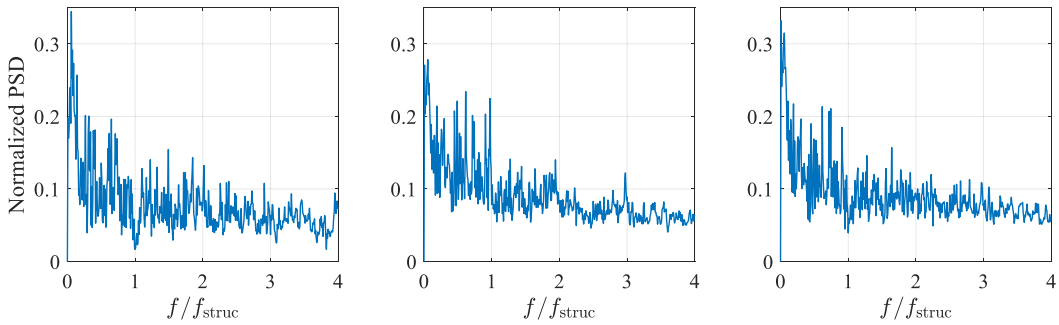

Fig. 13. Summed normalized PSDs of the ice force on the SDOF oscillators in the time interval 20–40 s. A clear trough in the ice force PSD occurs at the structure natural frequencies in the measured forces. This phenomenon is not visible in the simulated ice forces with no force-velocity gradient, and only a small power dip is visible in the simulated forces with a positive force-velocity gradient.

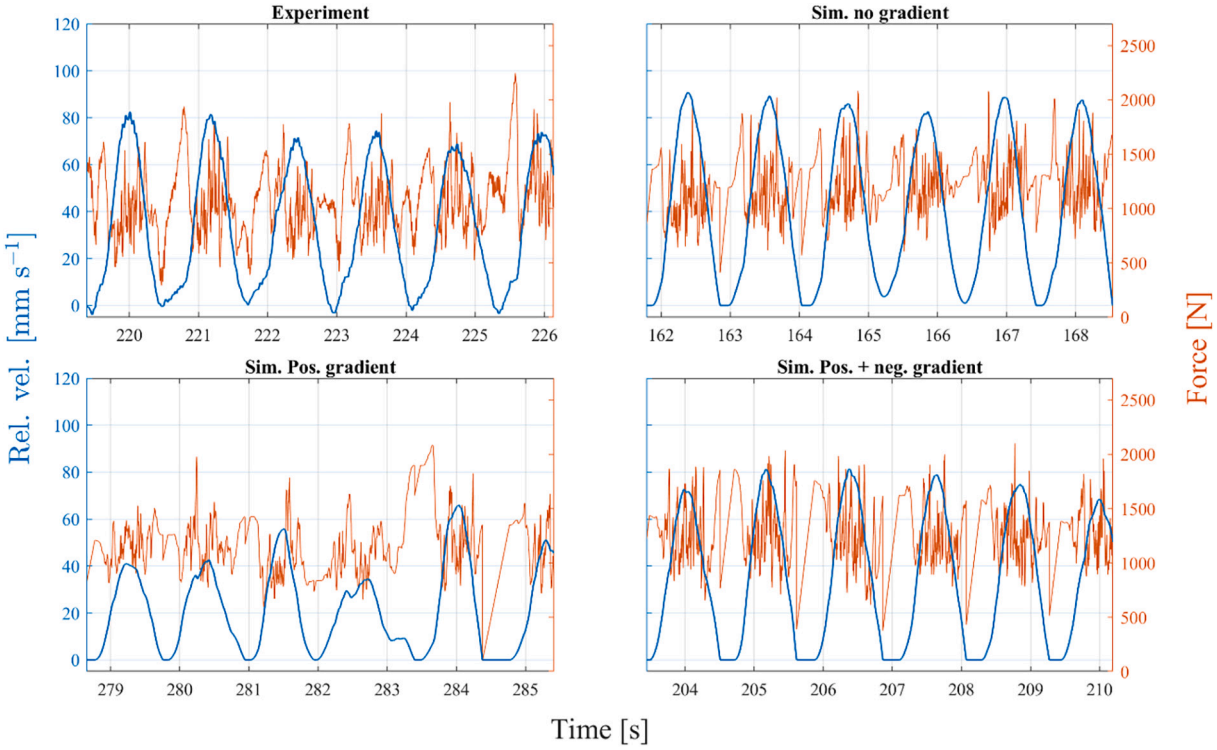

Fig. 14. Time-domain comparison of experimental and simulation results for the first cycles after FLI initiation.

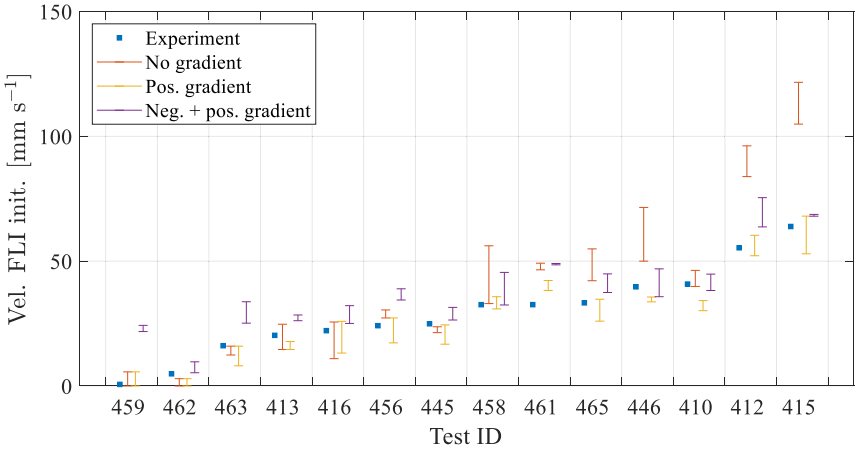

Fig. 15. Ice drift speed at which FLI starts to occur. Comparison of experiments (blue) and simulations. (For interpretation of the references to colour in this figure legend, the reader is referred to the web version of this article.)

The primary finding from the measured and simulated FLI initiation speeds is that, for most of the tested oscillator properties, the consideration of a negative ice force-velocity gradient is not necessary to correctly predict the FLI initiation speeds as observed in the tests. Rather, instead of needing the negative effective damping that would result from the negative force-velocity gradient, the positive force-velocity gradient observed at higher interaction velocities must be included to prevent an overprediction of FLI initiation speeds. This result indicates that, in the ice tank tests analysed in this study, FLI initiation is primarily driven by the properties of the ice force-displacement signal and, following from that, the frequency content of the force-time signal.

Fig. 16 shows the mean structural displacement amplitudes for the first 12 cycles after initiation of FLI. The simulation results show that once the interaction is in the FLI regime, considering only the positive force-velocity gradient at high relative velocities leads to an underestimation of the structural vibration amplitude. The negative force-velocity gradient at low velocities affects the interaction behaviour during FLI, and the consideration of this effect leads to a better prediction of the structural vibration amplitudes during FLI.

Fig. 17 shows the PSDs of ice force for the first 12 structural vibration cycles after FLI initiation. The PSD plots are frequency normalized by the peak displacement frequency (f_{disp}) over the evaluated time interval for each separate experimental or simulated signal. Then, the frequency-normalized PSDs are area-normalized by dividing by the area under the PSD curve of the experimental forces. In the experimental results (left), forcing frequency peaks occur at the peak displacement frequency and the higher harmonics of that frequency. In the simulated results with only a positive force-velocity gradient (middle), low peaks still occur at the structural displacement frequency and its higher harmonic, but the peaks are much less pronounced. In the simulation with positive and negative force gradient, clear forcing frequency peaks again occur at the peak displacement frequency and its higher harmonics.

8. Analysis and discussion of test results in the IC regime

The peak ice forces during IC loading cycles are evaluated for the range of tested SDOF oscillators and compared to the rigid structure observations. For this part of the study, the simple model is no longer applied as the interaction during IC proves too complex to capture with the model used in Section 7. Fig. 18 shows a typical IC load cycle as observed in the experimental data. This load cycle occurred in the base case test with ID 410 and indicates the peak force F_p and the relative velocity.

Fig. 19 distinguishes the results for the peak forces observed on the different indenters for two test days compared to rigid indenter tests on the same days. The dots show the peak forces during IC on the SDOF structures. The bars show the 95% confidence bounds (mean ± 2 standard deviations) of the peak forces measured during the rigid structure tests (peaks were determined from the force-time series on the rigid structures by applying a threshold value of the mean plus one standard deviation and a minimum peak prominence of 300 N). It is found that the peak force dependence on relative velocity for the SDOF structures shows the same trend as the peak force dependence on indentation speed for rigid structures. This indicates the importance of relative velocity and the negative force-velocity dependence at low speed for the development of intermittent crushing, making it not a purely brittle process as sometimes postulated.

9. Conclusions

This study analyses data from ice basin tests with a vertically sided cylindrical pile. Tests with a 'rigid' structure and with a series of SDOF oscillators were analysed. First, the properties of the ice forces measured on the rigid structure for a series of ice drift speeds were analysed. Then, the analysis focussed on the ice force characteristics relevant in the continuous brittle crushing and frequency lock-in regimes, and to the transition from continuous brittle crushing to frequency lock-in. Finally, we studied properties of the time-domain forces and structural response during intermittent crushing.

The analysis of ice forces from the rigid structure tests shows that the frequency content of the measured forces, when parameterized by its median frequency, is linearly related to the ice drift speed. This relationship indicates that the spatial frequency spectrum of the ice force is independent of the ice drift speed. The mean and standard deviation of the ice force are velocity dependent. At low ice drift speeds, these reduce with increasing drift speed, whereas at higher ice drift speeds there are indications these increase with increasing ice drift speed. The transition from a negative mean force-velocity gradient to a positive one occurred at an ice drift speed of approximately 20 mm s^{-1} in the tests performed.

The phenomena responsible for the initiation of frequency lock-in when the ice drift speed reduces from high to low are investigated by comparing the experimental results to simulated interaction results. The simulations isolate specific ice force characteristics observed in the rigid structure tests, such that the relative contributions of the different force characteristics can be considered. The characteristics included in the simulations are 1) measured force-displacement signals from rigid structure tests, 2) the positive force-velocity gradient observed for rigid structures at high speed, and 3) the negative force-velocity gradient observed for rigid structures at low speed.

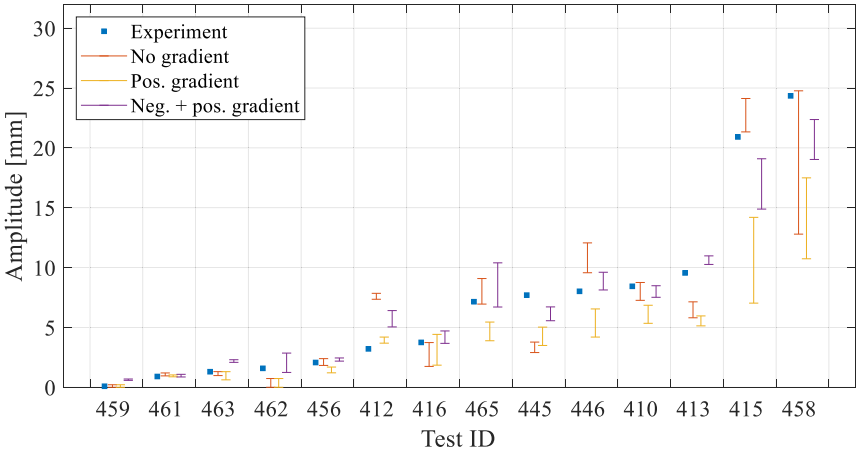

Fig. 16. Mean structural displacement amplitudes of first 12 structural vibration cycles after FLI initiation, comparison of experiments (blue) and simulations (if lock-in did not occur, the amplitude value is 0). (For interpretation of the references to colour in this figure legend, the reader is referred to the web version of this article.)

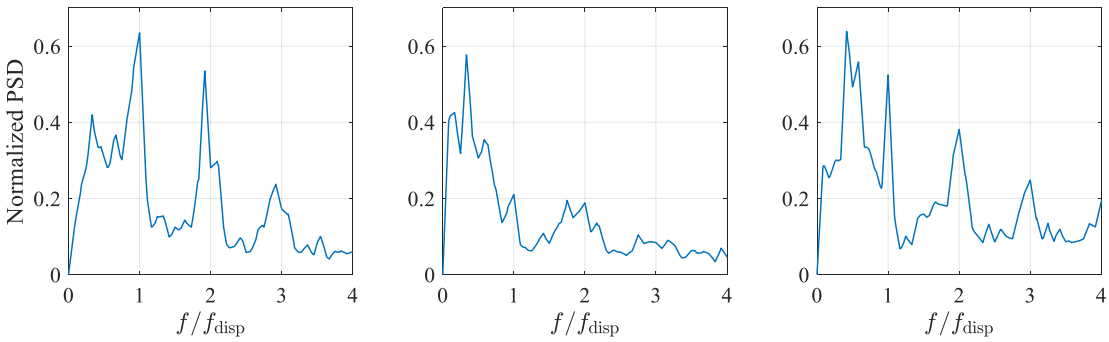

Fig. 17. Normalized and summed PSDs of ice forces during the first 12 cycles of FLI, measured forces (left) against simulated forces with only a positive force-velocity gradient (middle) and simulated forces with a positive and negative force-velocity gradient (right).

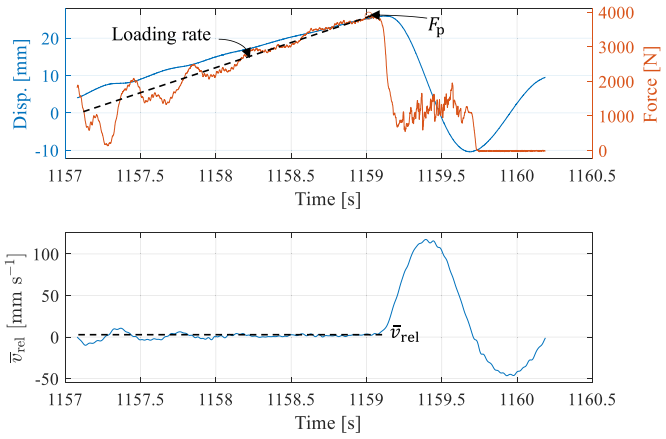

Fig. 18. Single cycle of IC, experimental data from base case test ID 410.

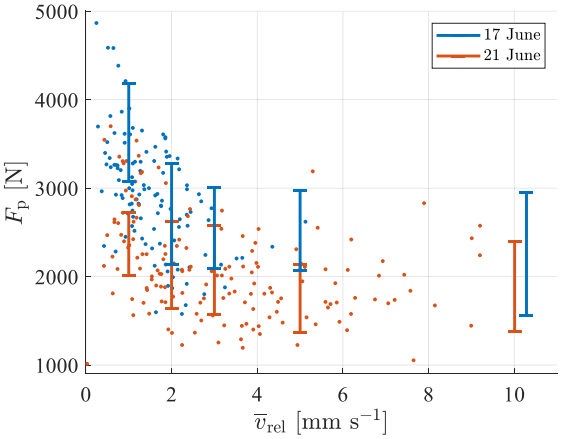

Fig. 19. Peak forces as a function of relative velocity during the load build-up phase in comparison to the peak forces measured during the rigid structure tests, distinguishing between the two days on which the tests were performed.

Comparison of simulation results to experimental data shows that the positive force-velocity gradient at higher ice drift speeds must be considered to capture the structural dynamics during continuous brittle crushing as measured during the experiments. This interaction effect at high ice drift speeds would not be captured by a frequency-domain analysis using the power spectral density of the random ice action, as proposed in ISO19906 (ISO, 2019) for the continuous brittle crushing regime. Such an analysis would lead to an over-estimation of the dynamic response of the structure.

The ice drift speeds at which frequency lock-in is initiated in the experiments are compared against the numerical simulation results. The simulations in which only the positive force-velocity gradient is considered predict well the frequency lock-in initiation drift speeds measured in the experiments during deceleration tests where the transition from continuous brittle crushing to frequency lock-in develops. This indicates that the negative force-velocity gradient at low ice drift speeds is not the primary mechanism responsible for this initiation. The transition from intermittent crushing to frequency lock-in has not been studied, and could be more susceptible to the negative force-velocity gradient.

After initiation of frequency lock-in, the experimental results indicate that the negative force-velocity gradient at low interaction velocities starts to play a role in the dynamic interaction between ice and structure. Simulations excluding this gradient under-predict the structural vibration amplitudes after frequency lock-in initiation.

The experimental data and analysis show that the spatial frequency content of ice forcing and negative force-velocity gradient on a rigid structure play a role in the dynamic interaction with compliant structures, but these are not sufficient to fully explain the observed ice-structure interaction. Modelling the interaction process purely based on one or a combination of these assumptions, which is still common in many numerical studies, is therefore not recommended.

Finally, analysis of the experimental data in the intermittent crushing regime shows that the peak forces are loading-rate dependent, and that the peak force trends measured in the 'rigid' structure tests match well with the IC peak force trends. This indicates the importance of relative velocity and the negative force-velocity dependence at low speed for the development of intermittent crushing, making it not a purely brittle process as sometimes postulated.

Data availability

The ice basin test data analysed in this study is available through Hendrikse et al. (2021): https://doi.org/10.4121/17087462.v1.

Funding

This work was supported by TKI-Energy by the 'Toeslag voor Topconsortia voor Kennis en Innovatie (TKI's)' of the Dutch Ministry of Economic Affairs and Climate Policy. (grant reference: TKITOE_WOZ_1906_TUD_SHIVER).

CRediT authorship contribution statement

Marnix van den Berg: Methodology, Software, Formal analysis, Investigation, Data curation, Writing – original draft, Visualization. **Cody C. Owen:** Formal analysis, Investigation, Writing – review & editing. **Hayo Hendrikse:** Conceptualization, Investigation, Writing – review & editing, Supervision, Project administration, Funding acquisition.

Declaration of Competing Interest

The authors declare that they have no known competing financial interests or personal relationships that could have appeared to influence the work reported in this paper.

Acknowledgements

The authors thank the participating organizations in the SHIVER project: TU Delft, Siemens Gamesa Renewable Energy, and Aalto University, for supporting this work.

We further thank Jeroen Koning, Kees van Beek and the colleagues from DEMO at TU Delft for the design and manufacturing of the mechanical parts of the test setup. We thank the crew of the Aalto Ice Tank: Teemu Päivärinta, Lasse Turja and Sampo Hanhirova, for their help in preparation and installation of the setup and execution of the tests. And our colleagues Tim Hammer, Tom Willems and Nick Ebben for the days in the cold executing the experiments.

Appendix A. Appendix

Table 3
Tests with a rigid structure considered in this study.

ID	Run name	v [mm s^{-1}]	ID	Run name	v [mm s^{-1}]	ID	Run name	v [mm s^{-1}]
379	1706_1	100	466	2106_9	100	488	2306_1	1
380	1706_1	1	467	2106_9	1	489	2306_1	40
418	1706_10	100	468	2106_9	40	490	2306_1	2
419	1706_10	1	469	2106_9	2	491	2306_1	150
420	1706_10	40	470	2106_9	150	492	2306_1	5
421	1706_10	2	471	2106_9	5	493	2306_1	60
422	1706_10	150	472	2106_9	60	494	2306_1	3
423	1706_10	5	473	2106_9	3	495	2306_1	20
424	1706_10	60	474	2106_9	20	496	2306_1	10
425	1706_10	3	475	2106_9	10	656	2106_1	100
426	1706_10	20	476	2106_9	0.1	657	2106_1	1
427	1706_10	10	487	2306_1	100			

Table 4
Tests with SDOF oscillators considered in this study.

ID	Run name	v_{init} [mm s^{-1}]	Duration [s]	m [10^{3}kg]	ζ [%]	ω [rad s^{-1}]
410	1706_7	70	402	5.02	1.3	5.53
412	1706_8	100	283	0.99	1.3	12.63
413	1706_8	60	472	20.06	1.3	2.76
415	1706_9	150	252	1.25	1.3	5.53
416	1706_9	50	373	20.06	1.3	5.53
445	1706_11	80	350	5.02	10.6	5.53
446	1706_11	80	350	5.02	0.17	5.53
456	2106_6	60	472	5.02	1.3	12.63
458	2106_7	150	252	5.02	1.3	2.76
459	2106_7	50	373	5.02	1.3	37.5
461	2106_8	50	373	1.10	1.3	37.5
462	2106_8	50	373	200.6	1.3	2.76
463	2106_8	50	373	9.90	1.3	12.63
465	2106_9	70	402	5.02	1.3	5.53

References

Blenkarn, K.A., 1970. Measurement and analysis of ice forces on cook inlet structures. In: Offshore Technology Conference. Dallas, Texas.

Gagnon, R.E., 2012. An explanation for the Molikpaq May 12, 1986 event. Cold Reg. Sci. Technol. 82, 75–93. https://doi.org/10.1016/j.coldregions.2012.05.009.

Gagnon, R., 2021. Spallation-based numerical simulations of ice-induced vibration of structures. Cold Reg. Sci. Technol. 194, 103465. https://doi.org/10.1016/j.coldregions.2021.103465.

Hammer, T.C., van Beek, K., Koning, J., Hendrikse, H., 2021. A 2D test setup for scaled real-time hybrid tests of dynamic ice- structure interaction. In: Proc. 26th Int. Conf. Port Ocean Eng. Under Arct. Cond.

Hendrikse, H., Hammer, T.C., van den Berg, M., Willems, T., Owen, C.C., van Beek, K., 2021. Data from ice tank tests with vertically sided structures collected during the SHIVER project.. In: 4TU.ResearchData. Dataset. doi: https://doi.org/10.4121/17087462.v1.

Hendrikse, H., Nord, T.S., 2019. Dynamic response of an offshore structure interacting with an ice floe failing in crushing. Mar. Struct. 65, 271–290. https://doi.org/10.1016/j.marstruc.2019.01.012.

Hendrikse, H., Ziemer, G., Owen, C.C., 2018. Experimental validation of a model for prediction of dynamic ice-structure interaction. Cold Reg. Sci. Technol. 151, 345–358. https://doi.org/10.1016/j.coldregions.2018.04.003.

Hendrikse, H., Hammer, T.C., Owen, C.C., van den Berg, M., van Beek, K., Polojärvi, A., Puolakka, O., Willems, T., 2022a. ICE BASIN TESTS FOR ICE-INDUCED VIBRATIONS OF OFFSHORE STRUCTURES IN THE SHIVER PROJECT. In: Proceedings of the ASME 2022 41st International Conference on Ocean, Offshore and Arctic Engineering OMAE2022-78507.

Hendrikse, H., Hammer, T.C., van den Berg, M., Willems, T., Owen, C.C., van Beek, K., Ebben, N.J.J., Puolakka, O., Polojärvi, A., 2022. Experimental data from ice basin tests with vertically sided cylindrical structures. Data in Brief 41, 107877. https://doi.org/10.1016/j.dib.2022.107877.

Huang, Y., Shi, Q., Song, A., 2007. Model test study of the interaction between ice and a compliant vertical narrow structure. Cold Reg. Sci. Technol. 49, 151–160. https://doi.org/10.1016/j.coldregions.2007.01.004.

ISO, 2019. ISO 19906:2019 Petroleum and Natural Gas Industries - Arctic Offshore Structures.

ITTC, 2014. ITTC – Recommended Procedures and Guidelines – Test Methods for Model Ice Properties.

Kärnä, T., Muhonen, A., Sippola, M., 1993. Rate effects in brittle ice crushing. Proc. In: 12th Int. Conf. Port Ocean Eng. Under Arct. Cond. Hamburg, Ger, pp. 59–71.

Kärnä, T., Kamesaki, K., Tsukuda, H., 1999. Numerical model for dynamic ice-structure interaction. Comput. Struct. 72, 645–658. https://doi.org/10.1016/S0045-7949(98)00337-X.

Määttänen, M., 1978. On Conditions for the Rise of Self-Excited Ice-Induced Autonomous Oscillations in Slender Marine Pile Structures.

Matlock, H., Dawkins, W.P., Panak, J.J., 1969. A model for the prediction of ice-structure interaction. In: Offshore Technology Conference. Dallas, Texas.
Palmer, A., Qianjin, Y., Fengwei, G., 2010. Ice-induced vibrations and scaling. Cold Reg. Sci. Technol. 60, 189–192. https://doi.org/10.1016/j.coldregions.2009.11.005.
Sodhi, D.S., 1991. Ice - structure interaction during indentation tests. In: IUTAM-IAHR Symposium. St. John's, Newfoundland Canada, pp. 619–640. https://doi.org/10.1007/978-3-642-84100-2_31.
Sodhi, D.S., Morris, C.E., 1986. Characteristic frequency of force variations in continuous crushing of sheet ice against rigid cylindrical structures. Colg Reg. Sci. Technol. 12, 1–12.
Sodhi, D.S., Takeuchi, T., Nakazawa, N., Akagawa, S., Saeki, H., 1998. Medium-scale indentation tests on sea ice at various speeds. Cold Reg. Sci. Technol. 28, 161–182.
Takeuchi, T., Sakai, M., Akagawa, S., Nakazawa, N., Saeki, H., 2001. On the factors influencing the scaling of ice forces. In: IUTAM Symp. Scaling Laws Ice Mech. Ice Dyn, pp. 149–160.
Toyama, Y., Sensu, T., Minami, M., Yashima, N., 1983. Model tests on ice-induced self-excited vibration of cylindrical structures. In: Proc. 7th Int. Conf. Port Ocean Eng. Under Arct. Cond.
Yue, Q., Zhang, X., Bi, X., Shi, Z., 2001. Measurements and analysis of ice induced steady state vibration. In: Proc. 16th Int. Conf. Port Ocean Eng. Under Arct. Cond.
Ziemer, G., 2021. Ice-Induced Vibrations of Vertical Structures. Doctoral thesis. Technischen Universität Hamburg.